Lorentz Force-Driven Autonomous Janus Swimmers

Gerardo Salinas, Kostiantyn Tieriekhov, Patrick Garrigue, Neso Sojic, Laurent Bouffier, Alexander Kuhn

Lorentz force-driven autonomous Janus swimmers

Gerardo Salinas, Kostiantyn Tieriekhov, Patrick Garrigue, Neso Sojic, Laurent Bouffier, Alexander Kuhn*

University of Bordeaux, CNRS, Bordeaux INP, ISM, UMR 5255, F-33607 Pessac, France.

KEYWORDS Microswimmers; Lorentz force; Janus particles; Bipolar electrochemistry; Magnetohydrodynamics; Dynamic chirality

ABSTRACT: Autonomous swimmers have been intensively studied in recent years due to their numerous potential applications in many areas, ranging from biomedicine to environmental remediation. Their motion is based either on different self-propulsion mechanisms or on the use of various external stimuli. Herein, the synergy between the ion flux around self-electrophoretic Mg/Pt Janus swimmers and an external magnetic field is proposed as an efficient alternative mechanism to power swimmers based on the resulting Lorentz force. A strong magnetohydrodynamic effect is observed due to the orthogonal combination of magnetic field and spontaneous ionic currents, leading reciprocally to an increase of the swimmer speed by up to two orders of magnitude. Furthermore, the trajectory of the self-propelled swimmers can be controlled by the orientation of the magnetic field, due to the presence of an additional torque force caused by a vertical cation flux along the swimmer edges, resulting in predictable clockwise or anticlockwise motion. In addition, this effect is independent of the swimmer size, since a similar type of chiral motion is observed for macro- and microscale objects.

INTRODUCTION

Macro-, micro- and nano-swimmers have gained a considerable attention[1-5] due to their numerous potential applications, *e.g.* for sensing,[6,7] cargo delivery[8,9] and environmental remediation.[10-12] Motion of these devices can be powered by different self-propulsion mechanisms, such as bubble propulsion, Marangoni effect, self-diffusiophoresis and self-electrophoresis.[13-19] These mechanisms are based, among others, on the asymmetric release of bubbles, caused by a catalytic reaction, the presence of surface tension gradients and the self-generation of local chemical gradients or electric fields. In addition, motion can also be powered in a wireless non-invasive way by applying external stimuli, *e.g.* acoustic waves,[20] light[21] and electric field.[22,23] They are used to induce surface tension gradients, photoelectrochemical, photocatalytical or electrochemical decomposition of fuels, or to trigger electroosmotic propulsion.

A powerful alternative to induce and control motion is also the use of an external magnetic field.[24-28] In this case, depending on the swimmer design, translation of the object is achieved either by a simple pulling mechanism[11,29-31] or by primary rotational/undulating motion,[32] for which alternating magnetic fields are used.[33-36] However, these systems require the incorporation of ferromagnetic components in the swimmer architecture, which can be a constraint, and often also imply the use of a rather complex equipment. We propose here a straightforward alternative concept based on the induction of a local Lorentz force on the surface of self-electrophoretic swimmers. When a magnetic field ($\vec{B}$) is imposed perpendicular to a classic electrode surface, a Lorentz force, acting on the ionic currents at the edges, is produced and causes hydrodynamic convection.[37] This is a well-known phenomenon, called magnetohydrodynamic effect (MHD).[38,39] The generated force, orthogonal to $\vec{B}$, produces two types of MHD flow; a macro-MHD flow along the electrode edges and micro-MHD vortices on the surface of the electrode due to local inhomogeneities.[37] This effect has been extensively used for the electrodeposition of copper,[40,41] silver[42] and polyaniline[43] to produce chiral structures on the surface of electrodes. Since for swimmers based on self-electrophoresis, two coupled redox reactions occur spontaneously at the anodic and cathodic parts of the intrinsically bipolar device, ionic currents are induced.[16] In this work, we take advantage of the coupling of these spontaneous ionic currents with an orthogonal magnetic field to generate a horizontal macro-MHD flow, providing a substantially increased driving force to propel the swimmer. Furthermore, the fraction of ionic current that propagates along the swimmer edges generates an additional Lorentz force ($\vec{F}$), which allows controlling its trajectory.

Scheme 1. Schematic illustration of (a) the formation of the macro-MHD flow on the surface of the electrically coupled Pt and Mg electrodes and (b) a Janus swimmer with a representation of the associated chemical reactions, the spontaneous ionic currents, the magnetic field ($\vec{B}$) and the resulting horizontal Lorentz force ($\vec{F}$).

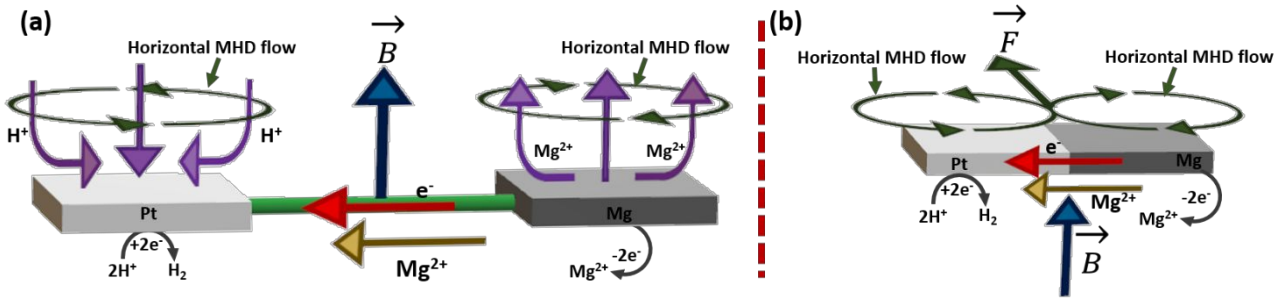

RESULTS AND DISCUSSION

The first step of this work is to illustrate the formation of two circular macro-MHD flow patterns in the proximity of a Mg/Pt Janus object which acts as an autonomous swimmer. The macroscopic version of such swimmers is obtained by attaching together 4 mm² magnesium (Mg) and platinum (Pt) foils that act as anode and cathode, respectively. However, in order to examine separately the processes occurring at the individual electrodes, they were first connected to each other by a 1 cm long metal wire (Scheme 1a, green line). This allows keeping them at a distance, large enough to avoid strong interferences. In acidic solutions, oxidation of Mg and reduction of H_3O^+ on Pt occur spontaneously with a standard redox potential difference of 2.34 V. These reactions produce a net flux of ions from the metal to the bulk of the solution in the case of Mg, and vice versa for Pt (Scheme 1a pink arrows). The electrons that need to be shuttled through the wire due to these spontaneous redox reactions are accompanied by a flow of ions, either Mg^{2+} cations from the Mg plate to the Pt plate, or OH^- ions from the Pt side to the Mg side. Most likely in reality a mixture of both will occur and thus for reasons of simplicity we only indicate in Scheme 1a the Mg^{2+} flux. As stated above, when simultaneously a magnetic field ($\vec{B}$) is applied perpendicular to the surface of both electrodes, the resulting Lorentz force produces two horizontal macro-MHD flow patterns along the edges of the electrodes (Scheme 1a, green arrows).[37]

In order to visualize this macro-MHD flow as a function of the orientation of the magnetic field, the two metal plates (*i.e.* Mg/Pt), connected by the wire, were immobilized at the bottom of a Petri-dish (*i.e.* static configuration), immersed in a 0.05 mM sodium dodecylbenzenesulfonate (SDS), 10 mM H_2SO_4 solution and placed at the center of a rectangular FeNdB magnet ($B \approx 200$ mT, $A = 98$ cm²). Glassy carbon beads ($Ø = 200 - 400$ µm) were spread on the air/water interface as tracking particles. Under these conditions, two circular hydrodynamic flow patterns can be observed, which follow the direction of the generated Lorentz force, as a function of the orientation of the magnetic field (Figure 1a and b, Video S1). A specular clockwise and anticlockwise motion of the tracking particles is established above the Pt and Mg surfaces, respectively, when the south pole of the magnet is facing up (Figure 1a). On the contrary, opposite trajectories of the tracking particles are seen when the orientation of the magnet is inverted (Figure 1b). To provide more quantitative information about the induced MHD flow, the trajectories and speed of a small number of glassy carbon beads (N = 4) were analyzed. The motion of four independent tracking particles on the air/water interface reveals again the characteristic clockwise and anticlockwise displacement (Figure 1c) with an oscillating speed value (Figure S1). The speed periodicity can be correlated with the position of the glassy carbon bead above the metal plate. As the tracking particles move along the outer part of the MHD flow, they have a relatively constant speed (1 mm/s). However, as soon as they get close to the region between the two plates (location of the connecting wire, green line in Figure 1) the speed increases, reaching a maximum of 4 mm/s. Passing this point, the speed starts to decrease again, eventually reaching its initial value.

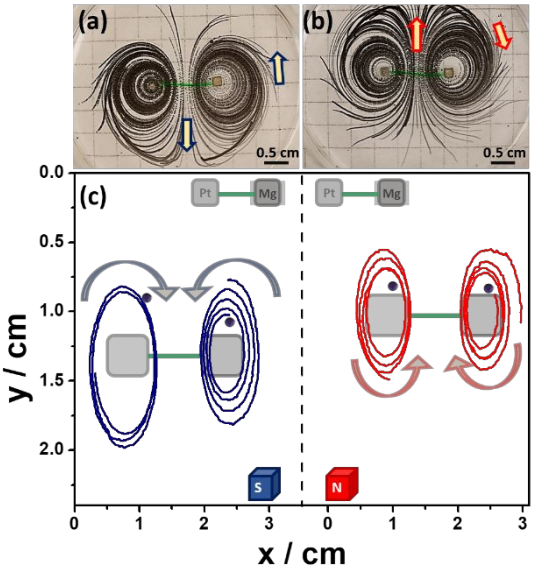

Figure 1. Trajectory of glassy carbon beads (d = 200 – 400 µm) moving on the air/water interface (0.05 mM SDS, 10 mM H_2SO_4) above the metal plates, as a function of the magnetic field orientation; (a) south pole up and (b) north pole up. (c) Tracking of the trajectories of four independent glassy carbon beads for the experiments in (a) and (b). The black dot indicates the initial point of the tracking particle. Global time of each experiment: 1 min.

After this first set of recordings, an analog series of experiments was performed with the macro-Janus swimmer depicted in Scheme 1b. Again, the device was first fixed in the middle of the Petri dish in order to analyze the MHD flow with the help of tracking particles. Theoretically, if the two metal plates are directly connected (no wire) the sum of the two individual MHD vortexes, at the center of the device, should produce an overall amplified horizontal driving force ($\vec{F}$) that *in fine* can be used for the propulsion of the swimmer with an increased efficiency (Scheme 1b).

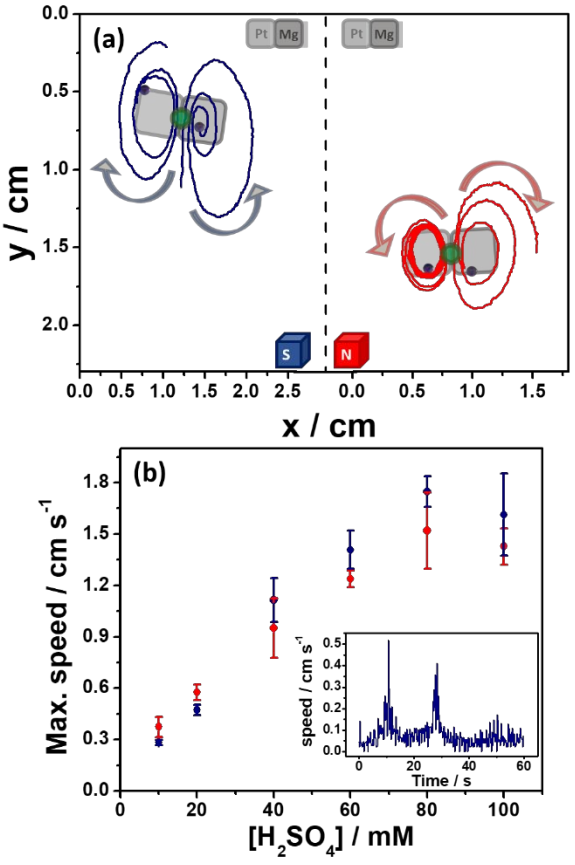

Figure 2. (a) Trajectory plot of two independent glassy carbon beads moving at the air/water interface of a 0.05 mM SDS, 20 mM H_2SO_4 solution, as a function of the magnetic field orientation (indicated in the figure). The black dot indicates the initial point of the tracking particle. (b) Maximum speed values as a function of the H_2SO_4 concentration. Inset: speed profile *versus* time of a glassy carbon tracking bead. Global time of each experiment: 1 min.

In the static configuration, the hydrodynamic effect of this force can be clearly seen when the set-up is placed at the center of the FeNdB magnet. Once again, glassy carbon beads were spread on the air/water interface as tracking particles. At low H_2SO_4 concentration (10 mM), the characteristic clockwise and anticlockwise circular patterns can be observed, as a function of the orientation of the magnetic field. As the H_2SO_4 concentration increases, the size of the hydrodynamic vortex increases (Figure S2). This is due to an enhancement of the thermodynamic driving force for the anodic and cathodic reactions, causing a faster macro-MHD flow. Nevertheless, the same clockwise and anticlockwise motion of the tracking particles, as a function of the magnetic field orientation, can also be observed at high H_2SO_4 concentration (100 mM) (Figure S2).

Motion of four independent tracking particles at the air/water interface of a 0.05 mM SDS, 20 mM H_2SO_4 solution was again analyzed in more detail (Video S2). It shows the characteristic clockwise and anticlockwise displacement as a function of the orientation of the magnetic field (Figure 2a) with an oscillating speed (inset in Figure 2b). As stated above, this periodicity can be correlated with the position of the glassy carbon bead above the static swimmer surface. Thus, along the macro-MHD flow in the periphery of the device, it moves with a relatively constant speed (0.5 mm/s), whereas it reaches a maximum (5 mm/s) close to the center of the swimmer (green spot in Figure 2a). By plotting the maximum speed as a function of the H_2SO_4 concentration, a linear correlation was obtained, reaching 17 mm/s as the highest speed value for 80 mM H_2SO_4 concentration (Figure 2b). The almost linear evolution of the speed is independent of the orientation of the magnetic field. It is worth mentioning that for the experiments at high acid concentrations, a black layer is formed on the surface of the Mg plate. SEM images and EDS analysis of the surface of the Mg electrode after the tracking experiments show the formation of a cracked layer, mainly composed of magnesium oxide and magnesium sulfate (Figure S3 and S4). This might explain the speed limit observed for high acid concentrations, but this layer does not passivate completely the electrode surface.

After these first series of experiments, allowing a characterization and visualization of the MHD flow patterns in a static configuration, we studied in the next step the behavior of a Janus swimmer with the same architecture, but allowing it to move (i.e. mobile configuration). Indeed, the presence of MHD flow, observed in the previous experiments, provides reciprocally a global driving force to propel the swimmer. The motion vector is oriented in the opposite direction with respect to the MHD flow, because what is important for global charge neutrality is the relative displacement. This means that either the swimmer is static and the liquid moves, or the swimmer moves with respect to the liquid, but with an inverted direction. For example, in the case of

the Janus swimmer depicted in the right panel of Figure 2a, the trajectory of the object would be downwards.

In addition to this global driving force resulting from the ions flowing from the bulk solution towards or away from the individual metal plate surfaces (Scheme 1a), there is an additional ion flux parallel to the surface of the device and especially along the edges (Scheme 1b). This lateral displacement of ions is necessary to compensate for the electrons flowing from the Mg to the Pt plate. It is reasonable to assume that Mg^{2+} ions are among the charge carriers involved in this process, as they are produced in large quantities on the Mg surface, and these cations will replace the H^+ ions consumed at the Pt surface. In the presence of the external magnetic field, this horizontal ionic current will generate an additional Lorentz force ($\vec{F}$), contributing to the overall driving force by inducing a torque (Scheme 2).

Scheme 2. Schematic illustration of the clockwise (top) and anticlockwise (bottom) motion of a self-propelled Janus swimmer.

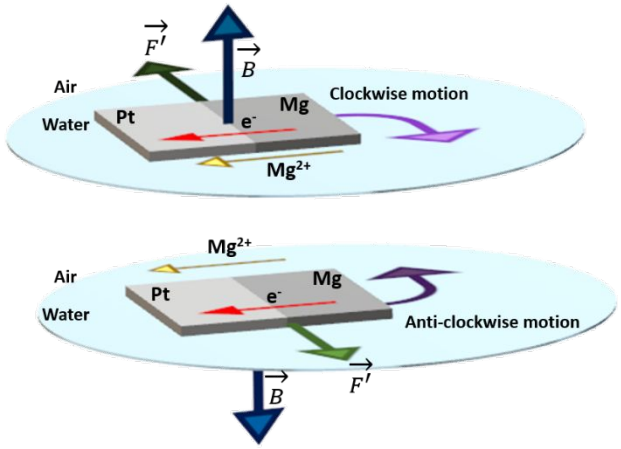

In order to visualize this torque force, the motion of four independent macro-Janus swimmers with a length of 4 mm was tested on the air/water interface of a 0.05 mM SDS, 40 mM H_2SO_4 solution. In the absence of magnetic field, the swimmer presents a stepwise motion at the 2-dimensional interface (random walk), due to the erratic formation of hydrogen bubbles (Figure S5a, Video S3 left side). When the north pole of the magnet is orientated upwards, a clockwise motion with an average speed of 10.2 ± 1.3 mm/s is recorded (Figure 3a, Videos S4 and S5 left side). When the orientation of the magnet is inverted (south pole upwards), an anticlockwise motion, with similar average speed (9.2 ± 0.7 mm/s), is observed (Videos S4 and S5 right side). These macro-swimmers show trajectories evolving as a function of time. In the beginning, when they are positioned in the very center of the magnet, where the field is quite homogeneous (Figure S6), a perfectly circular motion is observed, however with an opposite sense of rotation depending on the orientation of the magnetic field (Figure 3a, solid lines, Video S4). For experiments on a longer timescale, the swimmer will eventually explore positions where the magnetic field is no longer homogeneous (Video S5). The presence of such a magnetic field gradient drives the swimmer globally towards the outer zones of the magnet, following a trajectory composed of a sequence of semicircles, but conserving still the initial sense of rotation (Figure 3a, dashed lines), qualifying it as an object exhibiting dynamic chirality.

Finally, we were interested in testing whether the same alternative driving force can also be generated for smaller Janus swimmers. We therefore transposed the experiments to anisotropic Mg/Pt Janus particles, which were obtained by the spontaneous deposition of Pt black on one side of a 1.20 mm ± 0.07 mm Mg wire ($d \approx 0.5$ mm), when dipping it briefly in a H_2PtCl_6 solution (Inset in Figure 3b). The motion of these Janus swimmers was tested under the same conditions as previously. In the absence of magnetic field, the swimmer also shows an erratic stepwise motion, caused by bubble formation (Figure S5b and Video S3 right side). In the presence of the magnetic field the swimmer follows either a clockwise or anticlockwise circular trajectory (north or south pole facing up, respectively) with an average speed of 2.5 ± 0.1 mm/s (Figure 3b and Video S6).

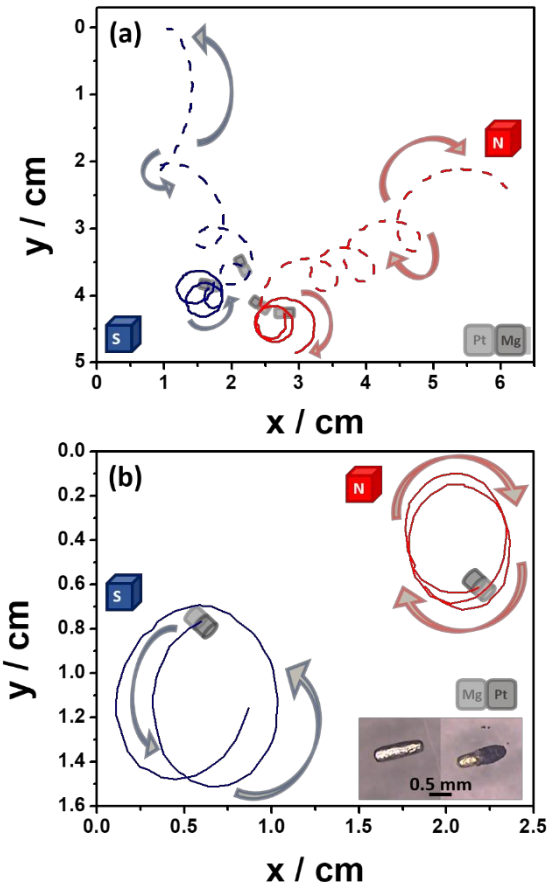

Figure 3. Trajectory plots of different Janus swimmers moving at the air/water interface of a 0.05 mM SDS, 40 mM H_2SO_4 solution, as a function of the magnetic field orientation (indicated in the figures). (a) Four independent macro-Janus swimmers (l = 4 mm); global time of the experiments: 4

seconds (solid lines) and 8 seconds (dashed lines). (b) Two micro-Janus swimmers (l = 1.22 mm ± 0.08 mm); global time of the experiments 15 seconds. Inset: Optical pictures of the Mg rods before (left) and after (right) asymmetrical modification in a 5 mM H_2PtCl_6 H_2O solution.

Since the above-mentioned additional torque originates from the flux of electrons and ions parallel to the edges of the swimmer, tuning this internal electron flow should have a pronounced effect on the swimmer trajectory. This can be tested by changing the percentage of Pt coverage. Two extreme cases were studied by covering either 20 % or 80 % of the wire surface with Pt black (Inset Figure 4 and Video S7). As can be seen, the swimmer with the smaller Pt coverage presents an only slightly curved clockwise or anticlockwise trajectory with an average speed of 1.2 ± 0.1 mm/s (Figure 4, dashed lines). In contrast, the device with a higher amount of Pt, shows well-defined circular motion with an average speed of 0.7 ± 0.1 mm/s. This pronounced difference is caused by the competition between the MHD flow and the additional torque force. When the majority of the electrons are directly used at the Mg surface for the local reduction of H_3O^+, due to a lack of Pt (20% of Pt), the MHD flow dominates the motion leading only to a slight curvature. However, when enough Pt is present (80% Pt coverage) to ensure the catalytic reduction of protons, which is much more favorable on Pt than on Mg from a kinetic point of view, an important fraction of the electrons liberated by the Mg corrosion will flow from Mg to Pt. Consequently, the additional torque will dominate the trajectory, producing perfectly circular motion (Figure 4, solid lines), and thus again a chiral trajectory.

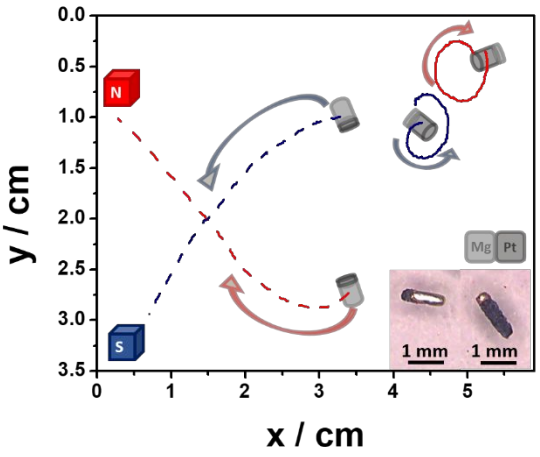

Figure 4. Trajectory plots of two independent Janus swimmers with different Pt coverages of 20 % (dashed line) and 80 % (solid line), moving at the air/water interface of a 0.05 mM SDS, 40 mM H_2SO_4 solution, as a function of the magnetic field orientation (indicated in the figures). Global time of the experiments: 30 seconds. Inset: Optical pictures of the Mg rods after asymmetric modification in a 5 mM H_2PtCl_6 H_2O solution (Left image 20% coverage, right image 80% coverage).

CONCLUSIONS

In conclusion, we have demonstrated the possibility to power Mg/Pt Janus swimmer propulsion using for the first time the effect of magnetohydrodynamic convection (MHD effect). The presence of tracking particles allows visualizing the formation of a macro-MHD flow, induced by the orthogonal combination of an external magnetic field and the ionic flux associated with the spontaneous redox reactions, occurring at the electrodes composing the swimmer. The synergy of the two macro-MHD flow patterns, present above the individual metals, allows generating an efficient global driving force able to propel the swimmer. An additional torque based on the Lorentz force caused by the flux of ions parallel to the swimmer surface, triggers a highly controllable clockwise or anticlockwise motion as a function of the orientation of the magnetic field. This dynamic chiral behavior is generic, since the same type of directional motion can be obtained for macro- and micro-devices. Finally, and most importantly, the proposed concept provides an easy and straightforward way to boost the propulsion speed of self-electrophoretic devices by up to two orders of magnitude with a permanent magnetic field, but without the need to integrate ferromagnetic components in the swimmer composition.

ASSOCIATED CONTENT

Supporting Information. Experimental procedures, additional tracking data and motion experiments, SEM images, EDS analysis and videos of the tracking particles and the macro and micro-swimmers (AVI) are included in the supporting information.

AUTHOR INFORMATION

Corresponding Author

*Email: kuhn@enscbp.fr

Author Contributions

The manuscript was written through contributions of all authors. All authors have given approval to the final version of the manuscript.

ACKNOWLEDGMENT

This work has been funded by the European Research Council (ERC) under the European Union's Horizon 2020 research and innovation program (grant agreement no 741251, ERC Advanced grant ELECTRA).

REFERENCES

(1) Wang J. *Nanomachines: Fundamentals and Applications*, Wiley, Hoboken, **2013**.
(2) Wang W.; Duan W.; Ahmed S.; Mallouk T. E.; Sen A. Small Power: Autonomous Nano- and Micromotors Propelled by Self-generated Gradients. *Nano Today* **2013**, *8*, 531–554
(3) Sanchez S.; Soler L.; Katuri J. Chemically Powered Micro- and Nanomotors. *Angew. Chem. Int. Ed.* **2015**, *54*, 1414–1444.

(4) Sengupta S.; Ibele M. E.; Sen A. Fantastic Voyage: Designing Self-Powered Nanorobots. *Angew. Chem. Int. Ed*. **2012**, *51*, 8434.
(5) Soto F.; Karshalev E.; Zhang F.; Fernandez de Avila B. E.; Nourhani A.; Wang J. Smart Materials for Microrobots. *Chem. Rev.* **2021**, *in press*, DOI: 10.1021/acs.chemrev.0c00999
(6) Duan W.; Wang W.; Das S.; Yadav V.; Mallouk T. E.; Sen A. Synthetic Nano- and Micromachines in Analytical Chemistry: Sensing, Migration, Capture, Delivery, and Separation. *Annu. Rev. Anal. Chem.* **2015**, *8*, 311-333.
(7) Patino T.; Porchetta A.; Jannasch A.; Llado A.; Stumpp T.; Schaffer E.; Ricci F.; Sanchez S. Self-Sensing Enzyme-Powered Micromotors Equipped with pH-Responsive DNA Nanoswitches. *Nano Lett.* **2019**, *19*, 3440-3447.
(8) Xu D.; Wang Y.; Liang C.; You Y.; Sanchez S.; Ma X. Self-Propelled Micro/Nanomotors for On-Demand Biomedical Cargo Transportation. *Small* **2020**, *16*, 1902464.
(9) Esteban-Fernandez de Avila B.; Angsantikul P.; Li J.; Lopez-Ramirez M. A.; Ramirez-Herrera D. E.; Thamphiwatana S.; Chen C.; Delezuk J.; Samakapiruk R.; Ramez V.; Zhang L.; Wang J. Micromotor-enabled Active Drug Delivery for in vivo Treatment of Stomach Infection. *Nat. Commun.* **2017**, *8*, 272.
(10) Rojas D.; Jurado-Sanchez B.; Escarpa A. "Shoot and Sense" Janus Micromotors-Based Strategy for the Simultaneous Degradation and Detection of Persistent Organic Pollutants in Food and Biological Samples. *Anal. Chem.* **2016**, *88*, 4153-4160.
(11) Gao W. W.; Feng X.; Pei A.; Gu Y.; Li J.; Wang J. Seawater-driven Magnesium Based Janus Micromotors for Environmental Remediation. *Nanoscale* **2013**, *5*, 4696-4700.
(12) Parmar J.; Vilela D.; Villa K.; Wang J.; Sanchez S. Micro- and Nanomotors as Active Environmental Microcleaners and Sensors. *J. Am. Chem. Soc*. **2018**, *140*, 9317–9331.
(13) Gao, W.; Uygun, A.; Wang, J. Hydrogen-Bubble-Propelled Zinc-Based Microrockets in Strongly Acidic Media. *J. Am. Chem. Soc*. **2012**, *134*, 897-900
(14) Salinas, G.; Dauphin, A. L.; Colin, C.; Villani, E.; Arbault, S.; Bouffier, L.; Kuhn, A. Chemo- and Magnetotaxis of Self-Propelled Light-Emitting Chemo-electronic Swimmers. *Angew. Chem. Int. Ed*. **2020**, *59*, 7508-7513
(15) Salinas, G.; Dauphin, A. L.; Voci, S.; Bouffier, L.; Sojic, N.; Kuhn, A. Asymmetry Controlled Dynamic Behavior of Autonomous Chemiluminescent Janus Microswimmers. *Chem. Sci*. **2020**, *11*, 7438-7443
(16) Wang Y.; Hernandez R. S.; Bartlett D. J.; Bingham J. M. Kline T. R.; Sen A.; Mallouk T. E. Bipolar Electrochemical Mechanism for the Propulsion of Catalytic Nanomotors in Hydrogen Peroxide Solutions. *Langmuir* **2006**, *22*, 10451–10456.
(17) Chi Q.; Wang Z.; Tian F.; You J.; Xu S. A Review of Fast Bubble-Driven Micromotors Powered by Biocompatible Fuel: Low-Concentration Fuel, Bioactive Fluid and Enzyme. *Micromachines* **2018**, *9*, 537.
(18) Zhou C.; Zhu P.; Tian Y.; Xu M.; Wang L. Engineering Micromotors with Droplet Microfluidics. *ACS Nano* **2019**, *13*, 6319–6329.
(19) Arnaboldi, S.; Salinas, G.; Karajic, A.; Garrigue, P.; Benincori, T.; Bonetti, G.; Cirilli, R.; Bichon, S.; Gounel, S.; Mano, N.; Kuhn, A. Direct Dynamic Readout of Molecular Chirality with Autonomous Enzyme Driven Swimmers. *Nat. Chem*. **2021**, *accepted*.
(20) Rao, K. J.; Meng, L.; Zheng, H.; Cai, F.; Wang, W. A Force to Be Reckoned With: A Review of Synthetic Microswimmers Powered by Ultrasound. *Small* **2015**, *11*, 2836-2846
(21) Fernández-Medina, M.; Ramos-Docampo, M. A.; Hovorka, O.; Salgueiriño, V.; Städler, B. Recent Advances in Nano- and Micromotors. *Adv. Funct. Mater*. **2020**, *30*, 1908283
(22) Bouffier, L.; Ravaine, V.; Sojic, N.; Kuhn, A. Electric Fields for Generating Unconventional Motion of Small Objects. *Curr. Opin. Colloid Interface Sci*. **2016**, *21*, 57–64
(23) Sharma, R.; Velev, O. D. Remote Steering of Self-Propelling Microcircuits by Modulated Electric Field. *Adv. Funct. Mater*. **2015**, *25*, 5512–5519
(24) Sanchez S.; Solovev A. A.; Harazim S. M.; Schmidt O. G. Microbots Swimming in the Flowing Streams of Microfluidic Channels. *J. Am. Chem. Soc*. **2011**, *133*, 701–703.
(25) Baraban L.; Makarov D.; Streubel R.; Mönch I.; Grimm D.; Sanchez S.; Schmidt O. G. Catalytic Janus Motors on Microfluidic Chip: Deterministic Motion for Targeted Cargo Delivery. *ACS Nano* **2012**, *6*, 3383–3389.
(26) Zhou, H.; Mayorga-Martinez, C.; Pane, S.; Zhang, L.; Pumera, M. Magnetically Driven Micro and Nanorobots. *Chem. Rev*. **2021**, *121*, 4999-5041
(27) Lee, S.; Kim, J. Y.; Kim, J.; Hoshiar, A.; Park, J.; Lee, S.; Kim, J.; Pane, S.; Nelson, B. J.; Choi, H. A Needle-Type Microrobot for Targeted Drug Delivery by Affixing to a Microtissue. *Adv. Healthc. Mater*. **2021**, *9*, 1901697.
(28) Chen, X. Z.; Liu, J. H.; Dong, M.; Müller, L.; Chatzipirpiridis, G.; Hu, C.; Terzopoulou, A.; Torlakcik, H.; Wang, X.; Mushtaq, F.; Puigmarti-Luis, J.; Shen, Q. D.; Nelson, B. J.; Pane, S. Magnetically Driven Piezoelectric Soft Microswimmers for Neuron-like Cell Delivery and Neuronal Differentiation. *Mater. Horiz*. **2019**, *6*, 1512-1516.
(29) Kline T.; Paxton W. F.; Mallouk T. E.; Sen A. Catalytic Nanomotors: Remote-Controlled Autonomous Movement of Striped Metallic Nanorods. *Angew. Chem. Int. Ed.* **2005**, *44*, 744–746.
(30) Zhao G.; Pumera M. Magnetotactic Artificial Self-Propelled Nanojets. *Langmuir* **2013**, *29*, 7411–7415.
(31) Paryab A.; Madaah-Hosseini H. R.; Abedini F.; Dabbagh A. Synthesis of Magnesium-based Janus Micromotors Capable of Magnetic Navigation and Antibiotic Drug Incorporation. *New J. Chem.* **2020**, *44*, 6947-6957.
(32) Dreyfus, R.; Baudry, J.; Roper, M. L.; Fermigier, M.; Stone, H. A.; Bibette, J. Microscopic Artificial Swimmers. *Nature* **2005**, *437*, 862-865.
(33) Gao W.; Sattayasamitsathit S.; Manesh K. M.; Weihs D.; Wang J. Magnetically Powered Flexible Metal Nanowire Motors. *J. Am. Chem. Soc*. **2010**, *132*, 14403–14405.
(34) Han K.; Shields IV C. W.; Velev O. D. Engineering of Self-Propelling Microbots and Microdevices Powered by Magnetic and Electric Fields. *Adv. Funct. Mater*. **2018**, *28*, 1705953.
(35) Qui T.; Lee T. C.; Mark A. G.; Morozov K. I.; Mügnster R.; Mierka O.; Turek S.; Leshansky A. M.; Fischer P. Swimming by Reciprocal Motion at Low Reynolds Number. *Nat. Commun*. **2014**, 5, 5119.
(36) Kadiri V. M.; Bussi C.; Holle A. W.; Son K.; Kwon H.; Schütz G.; Gutierrez M. G.; Fischer P. Biocompatible Magnetic Micro- and Nanodevices: Fabrication of FePt Nanopropellers and Cell Transfection. *Adv. Mater.* **2020**, *32*, 2001114
(37) Monzon L. M. A.; Coey J. M. D. Magnetic Fields in Electrochemistry: The Lorentz Force. A Mini-review. *Electrochem. Commun*. **2014**, *42*, 38-41.
(38) Mogi I.; Morimoto R.; Aogaki R. Surface Chirality Effects Induced by Magnetic Fields. *Curr. Opin. Electrochem*. **2018**, *7*, 1-6.
(39) Gatard V.; Deseure J.; Chatenet M. Use of Magnetic Fields in Electrochemistry: A Selected Review. *Curr. Opin. Electrochem.* **2020**, *23*, 96-105.
(40) Mogi I.; Watanabe K. Chiral Recognition of Amino Acids by Magnetoelectrodeposited Cu Film Electrodes. *Int. J. Electrochem*. **2011**, 239637
(41) Mogi I.; Aogaki R.; Takahashi K. Fluctuation Effects of

Magnetohydrodynamic Micro-Vortices on Odd Chirality in Magnetoelectrolysis. *Magnetochemistry* **2020**, *6*, 43
(42) Mogi I.; Watanabe K. Chirality of Magneto-electrodeposited Metal Film Electrodes. *Sci. Technol. Adv. Mater*, **2008**, *9*, 024210.
(43) Mogi I.; Watanabe K. Electrocatalytic Chirality on Magneto-electropolymerized Polyaniline Electrodes. *J. Solid State Electrochem*. **2007**, *11*, 751-756.